


## Probing the Degree of Heterogeneity within a Shear Band of a Model Glass

Muhammad Hassani,<sup>†</sup> Alexandra E. Lagogianni,<sup>‡</sup> and Fathollah Varnik<sup>\*,§</sup>  
 ICAMS, Ruhr-Universität Bochum, Universitätsstraße 150, 44780 Bochum, Germany

 (Received 12 April 2019; published 5 November 2019)

Recent experiments provide evidence for density variations along shear bands in metallic glasses with a length scale of a few hundred nanometers. Via molecular dynamics simulations of a generic binary glass model, here we show that this is strongly correlated with variations of composition, coordination number, viscosity, and heat generation. Individual shear events along the shear band path show a mean distance of a few nanometers, comparable to recent experimental findings on medium range order. The aforementioned variations result from these localized perturbations, mediated by elasticity.

DOI: [10.1103/PhysRevLett.123.195502](https://doi.org/10.1103/PhysRevLett.123.195502)

*Introduction.*—One of the most prominent manifestations of heterogeneity in metallic glasses is the shear-banding phenomenon [1,2]. Shear bands (SBs) are characterized by a local increase of excess free volume [3,4], temperature [5,6], and shear-induced softening [7,8]. They are usually formed via strain localization in narrow regions of 5–100 nm thickness [9,10] and constitute the main cause for the limited plasticity of metallic glasses and their catastrophic failure at room temperature [1]. The precursor [11,12] of shear bands in metallic glasses is the appearance of some regions that undergo local yielding, the so-called shear transformation zones (STZs) [13–15], which consist of 10–100 atoms that display large nonaffine atomic displacements and geometrically unfavored motifs [16,17]. The displacement and strain field around a STZ closely resembles that of an Eshleby inclusion [15,18–21] and in this description the shear band comes as the result of correlated and aligned quadrupoles [19,22–24].

Shear bands affect their vicinity within a range of up to hundreds of micrometers [25–27], inducing structural heterogeneity and fluctuations of local mechanical properties along the SB-propagation direction or path [28–31]. The local density also varies within the shear band [32–34] and is accompanied by deflections of the SB path [25,26].

However, albeit computer simulations provide useful insight on small length scales that experiments cannot always resolve, in this case, the complex nature of the shear bands [4] and the large length scales associated with local density variations [23] impeded a detailed quantitative analysis of this issue via computer simulations in 3D. Consequently, the origin of spatially varying patterns and the strong position dependent nature that properties exhibit along a shear band remains still an open question.

Here, we probe, via molecular dynamics simulations, the spatial variations of density and provide, for the first time, direct evidence for their correlations with coordination number, composition, excess free volume, plastic activity, local viscosity, and energy generation rate within and along

a shear band. We observe that every single quantity is closely connected to density, displaying variations on a similarly long length scale. In contrast, spatial arrangement of quadrupolar shear transformation events occurs on a significantly shorter length scale of a few nanometers. This supports the idea that STZs are localized events [13,24] which, when occurring in an elastic medium, can trigger long range perturbations [21]. At the same time, continuum mechanics models which assume a periodic alignment of quadrupolar stress-field perturbations need to be modified in order to account for this separation of length scales [23]. Interestingly, the average STZ distance agrees well with recent experimental reports on medium range order [35]. This highlights further the close connection between local structural features and the self-organization of shear transformation events [24,36].

A generic binary Lennard-Jones (LJ) glass former [37] is used (Supplemental Material [38]). Five statistically independent configurations are prepared. Each “sample” contains  $N \approx 2.5 \times 10^6$  particles in a thin slab with dimensions  $L_x \times L_y \times L_z = 2000 \times 10 \times 100$  (reduced LJ units). The  $L_x$  chosen here exceeds any earlier computationally resolved scale in 3D, even though such orders of magnitude for spatial variations within shear band are suggested by several experimental works [28–31]. Starting from an equilibrated liquid at a temperature of  $T = 2$  (the mode coupling critical temperature of the model is  $T_c \approx 0.43$  [39]), the system is quenched to a temperature of  $T = 10^{-4}$  close to the athermal limit [4]. Simple shear is then imposed with a rate of  $\dot{\gamma} = 10^{-4}$  by relative motion of the two parallel walls along the  $x$  direction [40]. The walls correspond to two frozen layers, each of three particle diameters thickness, and are separated by a distance of  $L_z = 100$ . Wall particles in this set of simulations have no thermal motion but move all together with a constant velocity of  $\pm U_{\text{wall}}$  along the  $x$  direction. Periodic boundary conditions are applied in the  $x$  and  $y$  directions. Using this protocol, we observe in each of the five independent samples the formation of a single

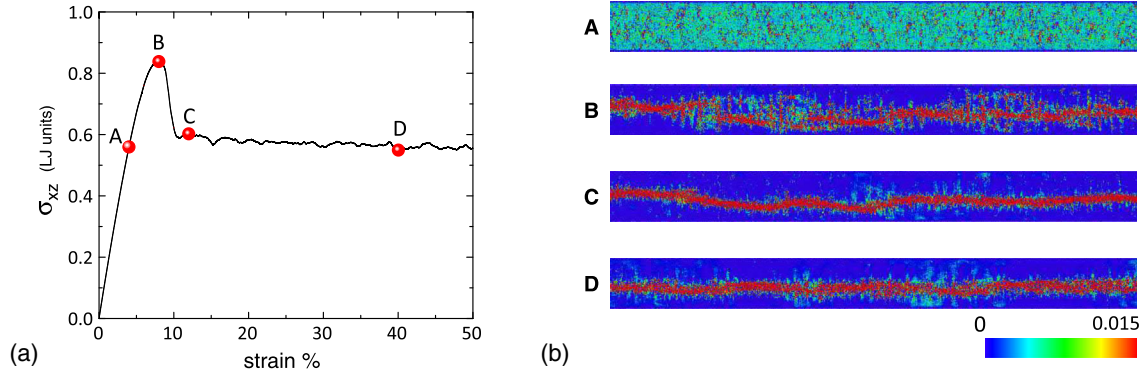


FIG. 1. (a) System averaged shear stress versus overall strain of the sheared glass in the athermal limit. Capital letters (*A*, *B*, *C*, *D*) indicate stress states for which the strain field is shown in the right panel. (b) Color coded atomic strain in the shear (*xz*) plane for different stress states depicted as full red spheres in the left panel. Strain is evaluated using particle displacements within finite time intervals corresponding to 1% global deformation. It contains both affine and nonaffine contributions.

and stable system-spanning shear band without the need of any notch or stress concentrator. In order to maximize the overall size of the *xz* plane while keeping the computational cost reasonable, the *y* dimension of the box is set to  $L_y = 10$ . This length is larger than the interaction cutoff length and the decay length of pair correlation function. Moreover, in the athermal limit considered here, finite size effects on dynamics play a subdominant role [41]. The system is sheared up to 50% overall strain. All the simulations reported here are performed using LAMMPS [42] while the 3D visualization and the color coding is done by the OVITO software [43]. This work presents the results of one independent initial configuration but the trends and conclusions have been tested and confirmed also for other four samples.

The deformed glassy system displays a typical stress-strain response [Fig. 1(a)] with a stress overshoot, which depends on the imposed strain rate [44], followed by a shear softening region until a quasi-steady state is reached that extends up to the largest strain investigated ( $\gamma_{\max} = 50\%$ ). The formation and the propagation of the shear band, demonstrated as high amounts of localized shear strain in a narrow region, is investigated via the calculation of the atomic strain from the infinitesimal Cauchy strain tensor, given as  $\epsilon_{i,\alpha\beta} = (1/2)[(u_{i,\alpha}/\partial\beta) + (\partial u_{i,\beta}/\partial\alpha)]$ . Here,  $\vec{u}_i$  is the (coarse-grained [45]) displacement vector of the *i*th particle within a globally imposed strain interval of  $\delta\gamma = 1\%$  and  $\alpha, \beta \in \{x, z\}$ .

Prior to yielding [point *A* in Fig. 1(a)], the atomic strain is rather homogeneously distributed [image *A* in Fig. 1(b)]. Progressively, as strain increases towards yielding, small isolated regions with accumulated atomic strain appear along the *x* axis (*B*) which later coalesce into a system-spanning shear band (*C* and *D*) with a wavy character along the SB-propagation direction. This is in remarkable agreement with recent experimental observations [25,26].

The local deflections are quantified by binning the shear band path along the SB-propagation direction with a bin width of 2.5 particle diameter. A geometric center (centroid)

is assigned to each bin, calculated by the Cartesian coordinates of its  $N_{\text{at}}$  constituent particles,  $\vec{r} = (1/N_{\text{at}}) \sum_{i=1}^{N_{\text{at}}} \vec{r}_i$  and averaged over sequential snapshots in the strain range  $\gamma = 10\% - 20\%$ . The thus obtained centroids form a “chain” that represents geometrically the SB path. For further analysis, an effective angle with respect to the *x* axis is also assigned to each SB segment. Sequential bins with negative or positive slope define a larger segment to which an average deflection angle is assigned. In agreement with experimental observations [25], this analysis reveals alternating descending and ascending segments, labeled here by Latin numbers and highlighted as white and black dashed lines [Fig. 2(a)]. It has to be mentioned that this is a simplified representation of the shear band, where the segments are displayed as straight lines. The actual segments, however, are slightly curved [see images *C* and *D* in Fig. 1(b)].

The local density changes inside and along the shear band path are spatially resolved by first introducing an atomic density  $\rho_i = (1/\Delta V) \sum_{j=1}^{N(i)} H(r_c - |\vec{r}_i - \vec{r}_j|)$ , and then evaluating its averages within each domain of interest. Here,  $H$  is the Heaviside step function and  $N(i)$  is the number of particles enclosed in a sphere of radius  $r_c$  (volume  $\Delta V$ ) around the *i*th particle ( $r_c =$  second minimum of the radial distribution function). The average over  $\rho_i$  for all particles within a SB segment centered at *x* provides the density  $\rho_{\text{SB}}(x)$ . The density difference between a SB segment and the matrix,  $\Delta\rho(x) \equiv \rho_{\text{SB}}(x) - \rho_M$  (Supplemental Material [38]), displays a strong position dependence and a wavy pattern that apparently averages out to a negative number indicative of a lower density within the shear band as compared to the matrix [23].

Density fluctuations show significant correlations with other physical quantities along the shear band. For example, we find a positive correlation with the deflection angle [Fig. 3(a)] in agreement with experimental observations [25,26]. Going beyond experiments, denser regions exhibit a higher average coordination number [Fig. 3(b)] and a lower percentage of large (*A*) particles [Fig. 3(c)]. Since in

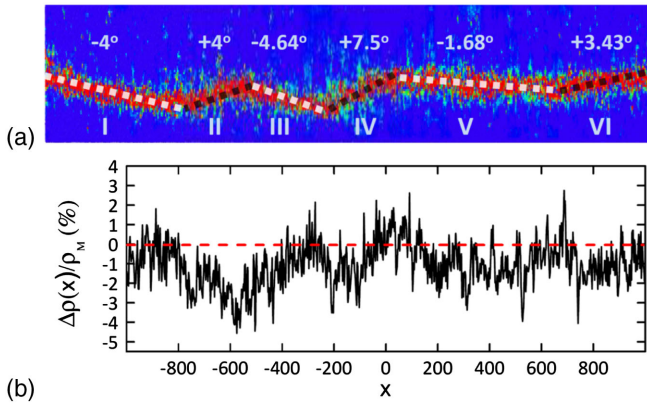


FIG. 2. (a) A typical zigzag type path of the shear band along the sample. White (black) dashed lines correspond to descending (ascending) segments. Note that the aspect ratio is not 1 : 1 but, to better highlight the wavy character of the SB path, the image is vertically enlarged. (b) Spatial variations of the relative density differences  $[\Delta\rho(x)/\rho_M]$  along the SB path.

general more unoccupied volume is available between larger spheres than among smaller ones, a region less rich in *A* particles impedes the creation of excess free volume [Fig. 3(d)], and therefore decreases the possibility of this region to undergo a nonaffine deformation [Fig. 3(e)], the latter quantified by the  $D_{\min}^2$  parameter [46]. In full agreement with this interpretation, dynamic viscosity, that defines the local resistance to plastic flow, is larger in regions of higher density [Fig. 3(f)]. And finally, more viscous regions coincide with higher amounts of locally dissipated energy [Fig. 3(g)].

Moreover, it has been proposed recently that the variations of density within shear band originate from an alignment of quadrupolar stress-field perturbations [23]. To address this issue, we build upon the analogy between the displacement field generated by a STZ and the corresponding continuum mechanics solution for a localized shear perturbation [15,21,48,49]. An analysis of the nonaffine displacement field reveals a sequence of STZs along the entire shear band path [Fig. 4(a)] with the same characteristics as the field generated by adjacent localized shear deformations in an isotropic elastic medium [Figs. 4(b)–4(d)]. We thus identify adjacent STZs and find a skew-symmetric distribution of their distance with a mean value of roughly six particle diameters (Fig. 5). A comparison to Fig. 2(b) reveals that this value is by roughly 2 orders of magnitude smaller than the length scale associated with density variations. For a comparison with experimental data [35], we choose the size of a particle to be a few angstroms and find the same scale separation between the wavelength of density variations and the distance between adjacent STZs (stress concentrators).

The results reported above have important consequences. (i) The agreement of density modulations in our simple glass model and experiments on bulk metallic glasses is remarkable [23,27,32] and underlines the generic character

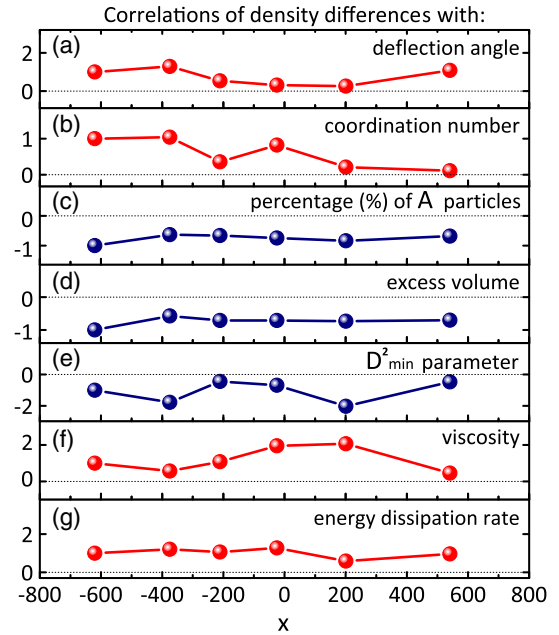


FIG. 3. Spatial correlations between *fluctuations* of  $\Delta\rho(x)$  ( $\Delta\rho(x) \equiv \rho_{\text{SB}}(x) - \rho_M$  = density difference between the shear band and the matrix) and those of other properties such as (a) the deflection angle, (b) the coordination number, (c) the composition or percentage (%) of *A* particles in  $A_x B_{100-x}$ , (d) the excess volume [4,47], (e) the  $D_{\min}^2$  parameter [46], (f) the dynamic viscosity, and (g) energy dissipation rate. In order to highlight whether a given quantity is positively or negatively correlated with density, the obtained correlation function is divided by the absolute value of the first (leftmost) data point. In the case of positive (negative) correlations, the data thus start with a value equal to +1 (−1). The main question here is then whether or not the data remain positive (negative) within the entire shear band. This is the case for all the quantities shown here (see Supplemental Material, Figs. S3–S9 [38]).

of this phenomenon. (ii) A debated topic in the metallic glass community concerns compositional changes within the shear band. Composition plays a paramount role in local atomic structure, which ultimately determines the material's properties and its response to mechanical load. Currently, however, the connection between composition and local deformation is far from being completely understood. To give just a few examples, we mention that while experiments on a (Al,Y)Fe metallic glass report a clear signature of compositional changes along the SB path [25,50], it has not been possible to detect such effects in Vitreloy 105 [35]. Liu and co-workers, on the other hand, report on compositional variations in a Zr-based metallic glass and their correlation with local volumetric changes [51]. In this debate, Fig. 3(c) shows that composition gradients are important players of the shear-banding phenomenon, independent of the specific glass former. This calls for new experiments, e.g., using radioactive tracers [52], to establish this generic character. (iii) There is currently also an active discussion on shear-induced



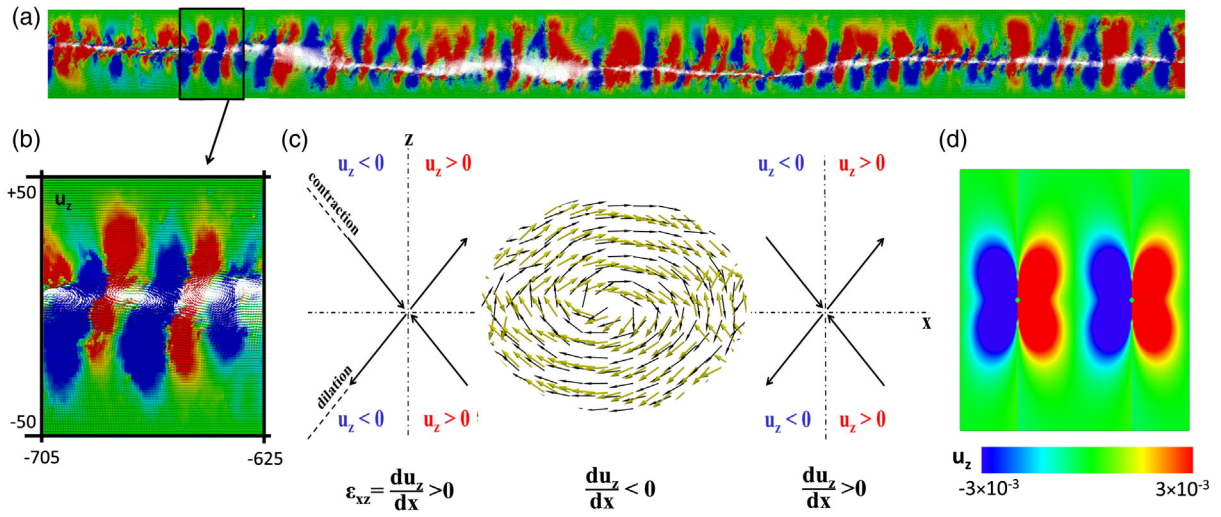


FIG. 4. (a) Scaled displacement vectors  $\vec{u}$  colored by their nonaffine component  $u_z$ . (b) Enlargement of two adjacent STZs of the SB. (c) The region between the two STZs shows the vortex structure of the displacement vectors (black). The vortex in gold is the continuum mechanics solution for the displacement vector field generated by two adjacent localized shear perturbations color coded in panel (d). The schematic drawing of the contraction and dilation axes in (c) serves to highlight the alternating sign of  $\epsilon_{xz}$  between two adjacent STZs (see Supplemental Material, Fig. S1 [38]).

heat generation within shear bands (see, e.g., [53–56] and references therein). Using the fact that MD simulations allow the access to atomic positions and forces, we show that the rate of heat generation is positively correlated with density fluctuations. Since the energy dissipation rate is the product of shear rate and stress, this observation reveals that the lower deformation rate in denser regions is overcompensated by an accompanying rise in stress. Thus, strong heat generation does not necessarily occur in the so-called “soft” regions, where larger shear deformation takes place but is rather localized in denser domains, capable of building larger stresses. An aspect of great interest for future studies here is in regard to local softening and rejuvenation effects due to heat generation. (iv) In contrast to the above discussed quantities, which vary on

the same (large) length scale as density, the distance between adjacent shear transformation events is by orders of magnitude smaller. This rules out attempts to relate oscillations of density to arrangements of STZs and calls for new models to adequately account for the connection between heterogeneities within shear band and the spatial organization of STZs.

Fruitful discussions with A. Zaccone are acknowledged. This study has been financially supported by the German Research Foundation (DFG) under the Projects No. VA205/16-2 and No. VA205/18-1. ICAMS acknowledges funding from its industrial sponsors, the state of North-Rhine Westphalia, and the European Commission in the framework of the European Regional Development Fund (ERDF).

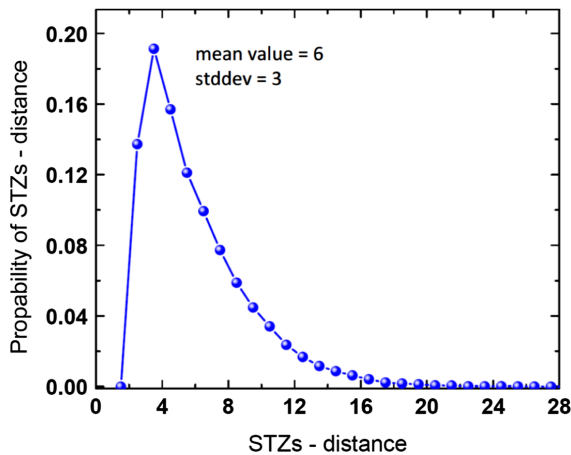


FIG. 5. (a) Distribution of the distance between two adjacent STZs along the shear band (reduced LJ units).

\*Corresponding author.  
fathollah.varnik@rub.de

†M. H. and A. E. L. contributed equally to this work.

- [1] L. Greer, Y. Cheng, and E. Ma, *Mater. Sci. Eng. R Rep.* **74**, 71 (2013).
- [2] R. Maaß and J. F. Löffler, *Adv. Funct. Mater.* **25**, 2353 (2015).
- [3] F. Spaepen, *Acta Metall.* **25**, 407 (1977).
- [4] M. Hassani, P. Engels, D. Raabe, and F. Varnik, *J. Stat. Mech.* (2016) 084006.
- [5] L. Battezzati and D. Baldissin, *Scr. Mater.* **59**, 223 (2008).
- [6] D. B. Miracle, A. Concustell, Y. Zhang, A. R. Yavari, and A. L. Greer, *Acta Mater.* **59**, 2831 (2011).
- [7] H. Bei, S. Xie, and E. P. George, *Phys. Rev. Lett.* **96**, 105503 (2006).

- [8] S. J. Wu, X. D. Wang, R. T. Qu, Z. W. Zhu, Z. Q. Liu, H. F. Zhang, and Z. F. Zhang, *Intermetallics* **87**, 45 (2017).
- [9] P. E. Donovan and W. M. Stobbs, *Acta Metall.* **29**, 1419 (1981).
- [10] S. Pauly, M. H. Lee, D. H. Kim, K. B. Kim, D. J. Sordelet, and J. Eckert, *J. Appl. Phys.* **106**, 103518 (2009).
- [11] P. P. Rico, D. Papageorgiou, A. Greer, and G. Evangelakis, *Acta Mater.* **135**, 290 (2017).
- [12] G. P. Shrivastav, P. Chaudhuri, and J. Horbach, *Phys. Rev. E* **94**, 042605 (2016).
- [13] A. S. Argon, *Acta Metall.* **27**, 47 (1979).
- [14] M. D. Demetriou *et al.*, *Phys. Rev. Lett.* **97**, 065502 (2006).
- [15] M. Hassani, P. Engels, and F. Varnik, *Europhys. Lett.* **121**, 18005 (2018).
- [16] J. Ding, S. Patinet, M. L. Falk, Y. Cheng, and E. Ma, *Proc. Natl. Acad. Sci. U.S.A.* **111**, 14052 (2014).
- [17] A. E. Lagogianni, G. Almyras, Ch. E. Lekka, D. G. Papageorgiou, and G. A. Evangelakis, *J. Alloys Compd.* **483**, 658 (2009).
- [18] J. D. Eshelby, *Proc. R. Soc. A* **241**, 376 (1957).
- [19] R. Dasgupta, H. G. E. Hentschel, and I. Procaccia, *Phys. Rev. Lett.* **109**, 255502 (2012).
- [20] F. Puosi, J. Rottler, and J. L. Barrat, *Phys. Rev. E* **89**, 042302 (2014).
- [21] M. Hassani, E. M. Zirdehi, K. Kok, P. Schall, M. Fuchs, and F. Varnik, *Europhys. Lett.* **124**, 18003 (2018).
- [22] R. Dasgupta, H. G. E. Hentschel, and I. Procaccia, *Phys. Rev. E* **87**, 022810 (2013).
- [23] V. Hieronymus-Schmidt, H. Rösner, G. Wilde, and A. Zacccone, *Phys. Rev. B* **95**, 134111 (2017).
- [24] D. Şopu, A. Stukowski, M. Stoica, and S. Scudino, *Phys. Rev. Lett.* **119**, 195503 (2017).
- [25] V. Schmidt, H. Rösner, M. Peterlechner, G. Wilde, and P. M. Voyles, *Phys. Rev. Lett.* **115**, 035501 (2015).
- [26] H. Rösner, M. Peterlechner, C. Kübel, V. Schmidt, and G. Wilde, *Ultramicroscopy* **142**, 1 (2014).
- [27] R. Maaß, K. Samwer, W. Arnold, and C. A. Volkert, *Appl. Phys. Lett.* **105**, 171902 (2014).
- [28] C. Liu and R. Maaß, *Adv. Funct. Mater.* **28**, 1800388 (2018).
- [29] P. Tsai, K. Kranjc, and K. M. Flores, *Acta Mater.* **139**, 11 (2017).
- [30] H. Wagner, D. Bedorf, S. Küchemann, M. Schwabe, B. Zhang, W. Arnold, and K. Samwer, *Nat. Mater.* **10**, 439 (2011).
- [31] D. Tönnies, K. Samwer, P. M. Derlet, C. A. Volkert, and R. Maaß, *Appl. Phys. Lett.* **106**, 171907 (2015).
- [32] F. Zhu, A. Hirata, P. Liu, S. Song, Y. Tian, J. Han, T. Fujita, and M. Chen, *Phys. Rev. Lett.* **119**, 215501 (2017).
- [33] M. Gross and F. Varnik, *Soft Matter* **14**, 4577 (2018).
- [34] S. Mandal, M. Gross, D. Raabe, and F. Varnik, *Phys. Rev. Lett.* **108**, 098301 (2012).
- [35] S. Hilke, H. Rösner, D. Geissler, A. Gebert, M. Peterlechner, and G. Wilde, *Acta Mater.* **171**, 275 (2019).
- [36] A. Cao, Y. Cheng, and E. Ma, *Acta Mater.* **57**, 5146 (2009).
- [37] W. Kob and H. C. Andersen, *Phys. Rev. Lett.* **73**, 1376 (1994).
- [38] See Supplemental Material at <http://link.aps.org/supplemental/10.1103/PhysRevLett.123.195502> for computational details, analytical solutions for single and double pre-sheared inclusions as well as additional simulation results on fluctuating quantities.
- [39] W. Kob and H. C. Andersen, *Phys. Rev. E* **51**, 4626 (1995).
- [40] F. Varnik, L. Bocquet, J. L. Barrat, and L. Berthier, *Phys. Rev. Lett.* **90**, 095702 (2003).
- [41] F. Varnik, J. Baschnagel, and K. Binder, *Phys. Rev. E* **65**, 021507 (2002).
- [42] S. Plimpton, *J. Comput. Phys.* **117**, 1 (1995).
- [43] A. Stukowski, *Model. Simul. Mater. Sci. Eng.* **18**, 085001 (2010).
- [44] F. Varnik, L. Bocquet, and J. L. Barrat, *J. Chem. Phys.* **120**, 2788 (2004).
- [45] C. Goldenberg, A. Tanguy, and J. L. Barrat, *Europhys. Lett.* **80**, (2007).
- [46] M. L. Falk and J. S. Langer, *Phys. Rev. E* **57**, 7192 (1998).
- [47] G. Voronoi, *J. Reine Angew. Math.* **1909**, 67 (1909).
- [48] B. Illing, S. Fritschi, D. Hajnal, C. Klix, P. Keim, and M. Fuchs, *Phys. Rev. Lett.* **117**, 208002 (2016).
- [49] M. Maier, A. Zippelius, and M. Fuchs, *Phys. Rev. Lett.* **119**, 265701 (2017).
- [50] S. Balachandran, J. Orava, M. Köhler, A. J. Breen, I. Kaban, D. Raabe, and M. Herbig, *Scr. Mater.* **168**, 14 (2019).
- [51] C. Liu, Z. Cai, X. Xia, V. Roddatis, R. Yuan, J. M. Zuo, and R. Maaß, *Scr. Mater.* **169**, 23 (2019).
- [52] D. Gaertner, K. Abrahams, J. Kottke, V. A. Esin, I. Steinbach, G. Wilde, and S. V. Divinski, *Acta Mater.* **166**, 357 (2019).
- [53] J. Lewandowski and A. Greer, *Nat. Mater.* **5**, 15 (2006).
- [54] S. K. Slaughter, F. Kertis, E. Deda, X. Gu, W. J. Wright, and T. C. Hufnagel, *APL Mater.* **2**, 096110 (2014).
- [55] P. Thurnheer, F. Haag, and J. Löffler, *Acta Mater.* **115**, 468 (2016).
- [56] Y. L. Tang, R. F. Wu, Z. M. Jiao, X. H. Shi, Z. H. Wang, and J. W. Qiao, *Mater. Sci. Eng. A* **704**, 322 (2017).